ELSEVIER

Journal of Fluids and Structures 25 (2009) 1102–1116

JOURNAL OF FLUIDS AND STRUCTURES

www.elsevier.com/locate/jfs

Utilization of bend–twist coupling for performance enhancement of composite marine propellers

Zhanke Liu, Yin L. Young*

Department of Civil and Environmental Engineering, Princeton University, Princeton, NJ 08544, USA

Received 22 February 2008; accepted 10 April 2009
Available online 27 May 2009

Abstract

Self-twisting composite marine propellers, when subject to hydrodynamic loading, will not only automatically bend but also twist due to passive bend–twist (BT) coupling characteristics of anisotropic composites. To exploit the BT coupling effects of self-twisting propellers, a two-level (material and geometry) design methodology is proposed, formulated, and implemented. The material design is formulated as a constrained, discrete, binary optimization problem, which is tackled using an enhanced genetic algorithm equipped with numerical and analytical tools as function evaluators. The geometry design is formulated as an inverse problem to determine the unloaded geometry, which is solved using an over-relaxed, nonlinear, iterative procedure. A sample design is provided to illustrate the design methodology, and the predicted performance is compared to that of a rigid propeller. The results show that the self-twisting propeller produced the same performance as the rigid propeller at the design flow condition, and it produced better performance than the rigid propeller at off-design flow conditions, including behind a spatially varying wake.

Keywords: Fluid–structure interaction; Bend–twist coupling; Design methodology

1. Introduction

Carbon fiber reinforced plastic (CFRP) composites, due to their high specific stiffness, high specific strength, anisotropic properties, among many other features, have been widely utilized in aerospace, aviation, marine, automotive, and civil engineering industries. Composite marine propellers made of CFRP have several advantages over conventional propellers made of nickel–aluminum–bronze (NAB) or manganese bronze (MB). Composite propellers have the potential to eliminate the galvanic cell set-up and hence can lower corrosion of steel ships and life-time costs (Kane and Smith, 2003). Composite propellers can also significantly reduce the weight, reduce maintenance cost, and increase the cavitation-inception speed (ITTC, 2005). Most importantly, composite propellers can be hydro-elastically tailored by exploiting the intrinsic bend–twist (BT) coupling effects of anisotropic composites to improve propeller performance.

Deformation coupling behavior of composites (e.g., extension–shear, bend–twist, and bend–extension coupling) can be utilized to tailor composite structures for performance enhancement. Many attempts have been made in the aerospace and aviation industries (Green, 1987; Yamane, 1992; Hwang and Gibson, 1993; Yamane and Peretz, 1993;

*Corresponding author. Tel.: +1 609 258 5426; fax: +1 609 258 0998.
E-mail address: yyoung@princeton.edu (Y.L. Young).

0889-9746/$ - see front matter © 2009 Elsevier Ltd. All rights reserved.
doi:10.1016/j.jfluidstructs.2009.04.005

Fukunaga and Sekine, 1994; Cho and Lee, 1998; Khan et al., 2000; Soykasap and Hodges, 2000; Khot and Zweber, 2003; VanGoethem and Radford, 2004). However, only limited work has been carried out on marine structures. An experimental study was presented in Gowing et al. (1998) for two composite elliptic hydrofoils made of carbon/epoxy skins with a syntactic foam core. Results showed that the tip deflections helped to delay cavitation inception due to reduced tip loading. However, the overall lift and drag coefficients remained unchanged. One of the first numerical studies of 3-D composite marine propellers was presented by Lin (1991). Effects of stacking sequence on the hydro-elastic behavior of composite propeller blades were assessed in Lin and Lin (1997). The possibility of maximizing the efficiency of composite propellers was numerically investigated in Lee and Lin (2004) and Lin and Lee (2004), but no formal design methodology was presented. More recently, the design, fabrication, and testing of 24-in model-scale pitch-adapting composite marine propellers were presented in Chen et al. (2006). The results confirmed that a properly designed flexible composite propeller can be more efficient, and cavitation inception can be significantly delayed compared to its rigid counterpart under highly loaded off-design conditions.

Although performance improvement of composite hydrofoils and propellers (compared to rigid counterparts) has been consistently demonstrated, a systematic design methodology is still lacking in the literature. To systematically exploit favorable hydro-elastic characteristics of composites, a systematic design methodology is needed to guide realistic applications. Hence, the objective of this work is to develop a design methodology to optimize the performance of self-twisting composite marine propellers by utilizing the bend–twist coupling characteristics of anisotropic composites.

2. Design strategies

2.1. J-dependency

Before presenting the design methodology, it is worthwhile to explain the flow dependency, represented by the advance coefficient $J \equiv U/2nR$, of the optimal pitch angle distribution of a propeller; R is the propeller blade radius, U is the mean axial inflow speed, and n is the propeller rotational frequency.

Consider a blade section at radius r along the span-wise direction as shown in Fig. 1. The nose-tail line is denoted as NT; $\beta(r) \equiv \tan^{-1}(U/2\pi nr) = \tan^{-1}(JR/\pi r)$ is the resultant inflow angle; $\phi(r)$ is the pitch angle defined with respect to the nose-tail line; $\alpha(r) = \phi(r) - \beta(r) = \phi(r) - \tan^{-1}(JR/\pi r)$ is the angle of attack. For a fixed pitch angle distribution, increasing advance coefficient J leads to decreasing angle of attack α; decreasing advance coefficient J leads to increasing angle of attack α. To maintain the optimal values for $\alpha_{opt}(r)$ at off-design conditions, $\phi_{opt}(r)$ should vary as a function of J. This is the J-dependency of the optimal pitch angle distribution.

2.2. Passive pitch adaptation

The direct implication of J-dependency is that a rigid propeller can only be optimal for a specific design flow condition J_0. Any deviation from the design flow condition J_0 will lead to a decrease in efficiency, since the resulting distribution of angle of attack as a function of the blade radius is suboptimal. The goal of using self-twisting propellers is to improve propeller performance in off-design conditions (including behind spatially varying wakes) via passive

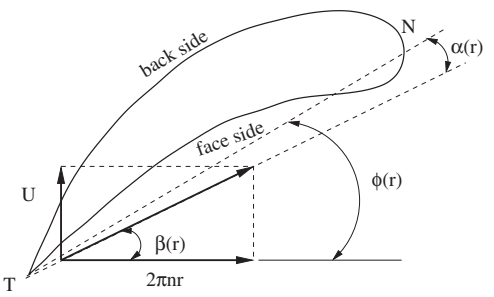

Fig. 1. Schematic drawing of flow around a blade section. Notice that the effective angle of attack $\alpha(r)$ is dependent upon the actual loading on the given blade section.

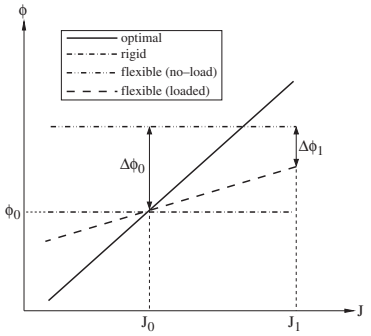

Fig. 2. Schematic drawing for pitch adaptation of self-twisting marine composite propellers. Notice that the tip pitch angle is chosen for illustration purposes.

pitch adaptation by exploiting the bend–twist coupling behavior of anisotropic composites. It should be noted that the pitch adaptation in the current work is passive and does not require an active device (e.g., mechanical driver/actuator) to mechanically alter the pitch profile. The passive pitch alteration is caused by the hydrodynamic bending moment and the intrinsic bend–twist coupling of anisotropic composites.

A schematic drawing of the adaptive pitch behavior of self-twisting propellers is shown in Fig. 2. For simplicity, the (blade) tip pitch angle has been used to represent the pitch angle profile of a linearly pitched propeller. Thus the radial dependency '(r)' is dropped hereafter.

The optimal tip pitch angle, $\phi_{\text{opt}} = \alpha_{\text{opt}} + \tan^{-1}(J/\pi)$, is denoted by the solid line in Fig. 2. To maintain the (constant) optimal angle of attack α_{opt}, the optimal pitch angle ϕ_{opt} must increase monotonically as a function of the advance coefficient J. Computationally, the optimal setting can be obtained by systematically varying the pitch angle distribution (represented by the tip pitch angle) and picking the particular value corresponding to the maximum efficiency for each individual advance coefficient J. This means that the optimal pitch angle profile is different for different Js. It implies that the rigid propeller, with a particular setting of pitch angle distributions, can only be optimal for a specific advance coefficient J_0.

For a rigid propeller, the tip pitch angle ϕ_0 is fixed over the range of Js, as denoted by the dash-dot line in Fig. 2; ϕ_0 is designed to be the same as ϕ_{opt} at the design flow condition J_0. For $J \neq J_0$ (off-design flow conditions), the rigid pitch angle distributions deviate from the optimal values.

The flexible self-twisting propeller is designed to be over-pitched in its undeformed (or no-load) configuration, as denoted by the dashed-double-dotted line in Fig. 2. The deformed (or loaded) pitch distribution of the self-twisting propeller is designed to match that of the rigid (or optimal) value at the design flow condition J_0, and to be near the optimal values at off-design conditions ($J \neq J_0$). The fundamental mechanism that enables the load-dependent pitch adaptation behavior will be explained in detail in Section 2.3.1. By virtue of this passive pitch adaptation behavior, the gap between the rigid and optimal configurations is bridged by the self-twisting propeller, which becomes the source of performance enhancement under off-design conditions. Notice that a linearly pitched propeller is chosen for simplicity. Similar ideas apply to propellers with nonlinear pitch distribution by tracking individual pitch angles along the span-wise direction.

2.3. Two-level design strategy

The goal of using self-twisting propellers is to improve propeller performance via passive pitch adaptation by exploiting the bend–twist coupling behavior of composites. To achieve this goal, two design criteria are set: (i) the flexible (self-twisting) propeller should perform the same as its rigid (non-twisting) counterpart under the design flow condition ($J = J_0$) at the same service speed; (ii) the flexible (self-twisting) propeller should perform better than its rigid (non-twisting) counterpart under a normal range of off-design flow conditions ($J \neq J_0$).

To achieve the design criteria, a two-level design strategy is proposed in the current work. The first level is the material design, which determines the proper material configuration that exhibits optimal pitch adaptation behavior. The second level is the geometry design, which determines the undeformed (no-load) geometry of the self-twisting propeller blade that deforms to match the geometry of the equivalent rigid propeller blade at the design flow condition ($J = J_0$). Details of the material and geometry designs are presented below.

2.3.1. Material design

The design objective is to obtain performance enhancement over the equivalent rigid propeller under off-design conditions by tailoring the load-dependent bend–twist deformations of the anisotropic composite blades. To achieve this objective, the first-level material design requires the material configuration to exhibit the optimal pitch adaptation behavior, which is the source of performance enhancement for a self-twisting propeller. This is equivalent to maximizing the slope k_p of the flexible self-twisting propeller as denoted by the dashed line in Fig. 2. The slope can be denoted as $k_p = (\Delta\phi_0 - \Delta\phi_1)/(J_1 - J_0)$, where $\Delta\phi_0$ and $\Delta\phi_1$ are the changes in tip pitch angle at advance coefficient J_0 and J_1, respectively. Based on hydrodynamic relations, $k_p = g(J_1 - J_0)\Delta\phi_0 \propto \Delta\phi_0$, where $g(\cdot)$ is a function that depends on the propeller geometry. Thus, the blade tip twist angle $\Delta\phi_0$ at the design advance coefficient J_0 is chosen as the objective function of the optimization problem. At the same time, there should be constraints on the material design to reduce the possibility of resonance and material failure (e.g., delamination and matrix cracking). One of the constraints is applied on the bending stiffness k; another constraint is the number of consecutive layers m. The constrained optimization problem can be formulated as

$$\max_{\vec{\theta}} \Delta\phi(\vec{\theta}), \quad k(\vec{\theta})/k_{\max} \geq \xi, \quad m(\vec{\theta}) \leq m_{\max}, \tag{1}$$

where $k_{\max}$ and $m_{\max}$ are the maximum bending stiffness and maximum allowable number of consecutive layers, respectively; ξ is the specified critical stiffness ratio. The mathematical formulation of the optimization problem can be simplified by introducing penalty parameters λ_1 and λ_2:

$$\max_{\vec{\theta}} \left\{ \Delta\phi(\vec{\theta}) \left[\frac{k(\vec{\theta})}{k_{\max}} \right]^{\lambda_1} \lambda_2^{m(\vec{\theta}) - m_{\max}} \right\}. \tag{2}$$

To simplify the presentation of the design philosophy, the material properties are assumed to be given, so that only the stacking sequence, represented by the vector $\vec{\theta}$ in Eq. (2), is allowed to vary. It should be noted that the current optimization scheme could easily be extended to allow for varying material properties and thickness distributions by introducing additional variables.

Eq. (2) is implemented using an enhanced genetic algorithm. Genetic algorithms have been widely used in optimization problems (Marques and Anderson, 2001; Ziaei-Rad and Ziaei-Rad, 2006; Howe, 2007). It is a subset of stochastic optimization methods modeled after the process of natural selection. It starts by a randomly selected first generation of individuals. Subsequent new generations are born out of mate selection, crossing-over, and mutation. Each individual is assigned a fitness value through function evaluation. The fittest individuals have a higher chance of reproduction, and are therefore more likely to pass on their genes to the next generation.

The most CPU-time intensive part of a genetic algorithm is the function evaluation. In the current work, it is to compute the propeller performance using the coupled FSI solver. To speed up the optimization process, the total number of function evaluations and/or the CPU time of each individual function evaluation should be reduced. To reduce the number of function evaluations, the genetic algorithm in the current work has been augmented with a binary tree memory algorithm (Kogiso et al., 1993, 1994). To speed up the convergence rate, local improvement (Kogiso et al., 1993, 1994) is added to the genetic algorithm. Both the binary tree memory and local improvement have been shown to significantly reduce the total number of function evaluations (Plucinski et al., 2007). In the design samples of the current work, two types of function evaluators, namely an analytical plate model and a numerical propeller fluid–structure interaction analysis solver, are tested and compared. Comparison shows that the analytical plate model can significantly reduce the CPU time and hence can be used as an auxiliary function evaluator. Details of these two function evaluators and performance comparison will be presented in Sections 3 and 4, respectively.

2.3.2. Geometry design

The geometry design follows after the material design. It involves solving the inverse problem where the deformed geometry under design flow conditions (or mean-load geometry) is known, but the undeformed geometry (or no-load geometry) is unknown. The objective of the geometry design is to determine the no-load (undeformed) geometry of the self-twisting propeller which will deform to the mean-load geometry at the design flow condition. The flow chart of the geometry design is shown in Fig. 3. In the flow chart, G_0 and G_N, respectively, refer to the deformed (mean-load) geometry and undeformed (no-load) geometry of the flexible self-twisting propeller under the design flow condition. The mean-load geometry G_0 is taken as the initial guess for the no-load geometry G_N. The intermediate deformed geometry G_1 due to fluid–structure interactions is then calculated via a numerical propeller analysis solver (more details are provided in Section 3.2). If $G_1 \neq G_0$, the no-load geometry is updated as $G_N = G_N - \lambda(G_1 - G_0)$. This loop is

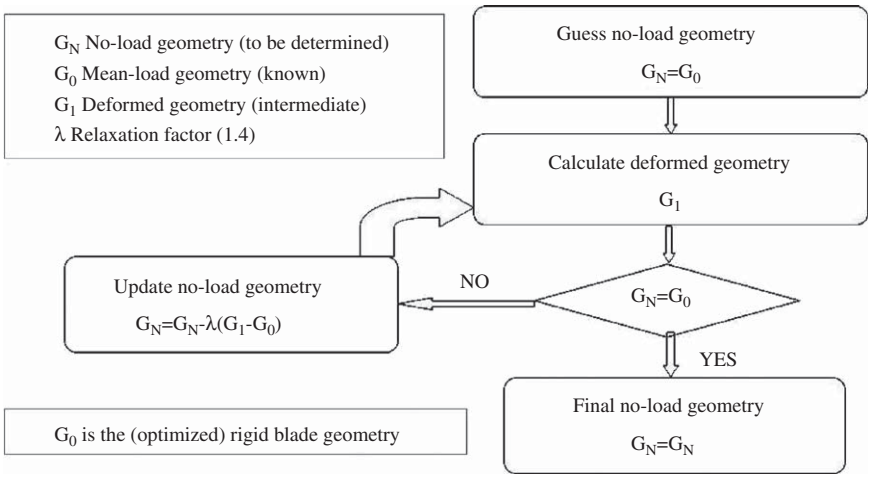

Fig. 3. Flowchart of the geometry design.

repeated until $G_1 = G_0$ and the latest G_N is taken to be the converged solution for the no-load geometry. To speed up convergence, an over-relaxation factor of $\lambda = 1.4$ is usually adopted.

Via the two-level design, the no-load geometry G_N will be deformed to the mean-load geometry G_0 at the design flow condition J_0. For $J > J_0$, the tip resultant inflow angle $\beta = \tan^{-1}(J/\pi)$ is higher than at J_0, which leads to lower angle of attack $\alpha = \phi - \beta$ than at J_0. The blade deformation at $J > J_0$ is less than that at J_0 due to lower hydrodynamic load, and hence the deformed pitch angle distribution of the flexible blade will be higher than its rigid counterpart. On the contrary, at $J < J_0$, the deformed pitch angle distribution of the flexible blade will be lower than its rigid counterpart due to higher hydrodynamic load. Graphical illustration of the resultant pitch adaptation behavior is schematically represented by the dotted line in Fig. 2. Notice that the solid line in the figure corresponds to the theoretical optimum defined by the pitch angle distribution that will maximize the rigid blade efficiency at individual Js. The theoretical optimal performance cannot be physically achieved using a rigid (non-twisting) propeller since the pitch angle distribution is fixed at all Js; however, they can be approached by a properly designed flexible propeller (self-twisting) via passive pitch adaptation as explained above.

3. Design tools

3.1. Analytical tool

To aid the conceptual design and to speed up the function evaluation in the optimization procedure, a simplified analytical model is developed. The composite propeller blade is simplified as a cantilevered plate subject to pure bending as shown in Fig. 4. The reason for examining this particular configuration is based on two considerations. The first consideration is that the behavior of a cantilevered plate subject to pure bending is similar to a propeller blade subject to hydrodynamic bending. The second is that for self-twisting composite marine propellers, the bend–twist coupling caused by material anisotropy is of utmost importance, and can be captured by the analytical prototype. There is no intention to obtain performance curves of realistic propellers, which have complex geometries (pitch, rake, skew, etc.), using the simplified analytical model. However, the analytical model can be used as an efficient function evaluator to speed up the selection of the optimal material configuration that maximizes the bend–twist coupling.

As shown in Fig. 4, the cantilevered plate is fixed at the root and is subject to a concentrated bending moment M at the free end. It has a length of a, width of b, and thickness of t. The length, width, and thickness directions are denoted by $\tilde{x}$, $\tilde{y}$, and $\tilde{z}$, respectively. The middle surface of the plate lies in the $\tilde{x}$–$\tilde{y}$ plane. The normal to the middle surface is in the $\tilde{z}$ direction. According to classical lamination theory (CLT), the flexural curvatures of a symmetric laminate as shown in Fig. 4 can be obtained as follows:

$$\kappa_{\tilde{x}} = d_{11}M, \quad \kappa_{\tilde{y}} = d_{12}M, \quad \kappa_{\widetilde{xy}} = d_{16}M, \tag{3}$$

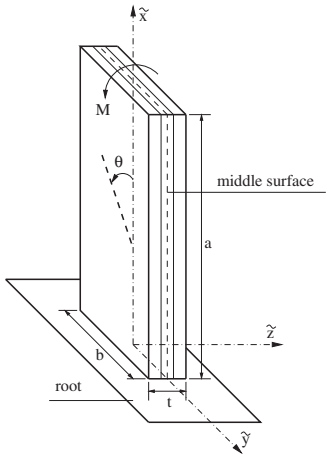

Fig. 4. Physical prototype of a cantilevered structure subject to pure bending.

where $\kappa_{\tilde{x}}$ and $\kappa_{\tilde{y}}$ are the bending curvatures of the middle surface, and $\kappa_{\widetilde{xy}}$ is the twisting curvature of the middle surface. The flexural compliance d_{ij} are related to the flexural stiffness D_{ij} as follows:

$$d_{11}=\frac{D_{22}D_{66}-D_{26}^2}{\Delta_D^s},\quad d_{12}=\frac{D_{16}D_{26}-D_{12}D_{66}}{\Delta_D^s},\quad d_{16}=\frac{D_{12}D_{26}-D_{16}D_{22}}{\Delta_D^s},$$
$$\Delta_D^s=D_{11}D_{22}D_{66}-D_{11}D_{26}^2-D_{22}D_{16}^2-D_{66}D_{12}^2+2D_{12}D_{16}D_{26}. \tag{4}$$

For a laminate of N layers, the flexural stiffness D_{ij} are defined as $D_{ij}\equiv\frac{1}{3}\sum_{k=1}^{N}(\bar{Q}_{ij})_k(z_{k+1}^3-z_k^3)$, where the $\bar{Q}_{ij}$ are the transformed reduced in-plane stiffness coefficients for a single lamina:

$$\begin{aligned}
\bar{Q}_{11}&=Q_{11}\cos^4\theta+2(Q_{12}+2Q_{66})\sin^2\theta\cos^2\theta+Q_{22}\sin^4\theta,\\
\bar{Q}_{22}&=Q_{11}\sin^4\theta+2(Q_{12}+2Q_{66})\sin^2\theta\cos^2\theta+Q_{22}\cos^4\theta,\\
\bar{Q}_{66}&=(Q_{11}+Q_{22}-2Q_{12}-2Q_{66})\sin^2\theta\cos^2\theta+Q_{66}(\sin^4\theta+\cos^4\theta),\\
\bar{Q}_{12}&=(Q_{11}+Q_{22}-4Q_{66})\sin^2\theta\cos^2\theta+Q_{12}(\sin^4\theta+\cos^4\theta),\\
\bar{Q}_{16}&=(Q_{11}-Q_{12}-2Q_{66})\sin\theta\cos^3\theta+(Q_{12}-Q_{22}+2Q_{66})\sin^3\theta\cos\theta,\\
\bar{Q}_{26}&=(Q_{11}-Q_{12}-2Q_{66})\sin^3\theta\cos\theta+(Q_{12}-Q_{22}+2Q_{66})\sin\theta\cos^3\theta.
\end{aligned} \tag{5}$$

In Eq. (5), θ is the ply orientation angle measured positive counter-clockwise from the plate's axial $\tilde{x}$ coordinate to the principle material fiber coordinate as shown in Fig. 4, and the Q_{ij} are the reduced in-plane stiffness coefficients of individual laminae:

$$Q_{11}=\frac{E_L}{1-\nu_{LT}\nu_{TL}},\quad Q_{12}=\frac{\nu_{LT}E_T}{1-\nu_{LT}\nu_{TL}},\quad Q_{22}=\frac{E_T}{1-\nu_{LT}\nu_{TL}},\quad Q_{66}=G_{LT}, \tag{6}$$

where L and T signify the local fiber and transverse directions, respectively; E_L and E_T are Young's moduli in the fiber and transverse directions, respectively; ν_{LT} is the Poisson ratio measuring strain in the T direction subject to uniaxial normal stress in the L direction; G_{LT} is the in-plane shear modulus.

The analytical plate model reveals that the intrinsic bend–twist coupling of anisotropic composites (characterized by $\kappa_{\widetilde{xy}}$ in Eq. (3)) is the governing mechanism that enable the blades to bend and twist when subject hydrodynamic bending, which is the primary source of performance enhancement of composite marine propellers. It has been successfully used in Liu and Young (2007) to study the correlations between the twisting rate, the pitch angle alteration, and efficiency improvement of realistic composite marine propellers. In the current work, its applicability as an efficient auxiliary function evaluator for the constrained optimization problem will be further demonstrated.

3.2. Numerical tool

Although the analytical tool is efficient to speed up the material optimization process, it cannot evaluate the performance curves for realistic composite propellers with complex geometry. The numerical tool used in the current

work is a 3-D propeller fluid–structure interaction analysis solver for the quasi-steady and transient analysis of flexible composite propellers. The numerical model is summarized below. Notice that the x-axis in the numerical model is defined to be the same as the propeller shaft axis. The positive direction points toward the downstream direction. More details of the formulation, numerical implementation, and validation studies can be found in Young and Liu (2007) and Young (2007, 2008).

Consider a marine propeller rotating at a constant angular velocity $\omega = 2\pi n$; the discrete equation of motion for the blade in the rotating blade-fixed coordinates system can be written as follows:

$$([\mathbf{M}] + [\mathbf{M}_H])\{\ddot{\mathbf{u}}\} + ([\mathbf{C}] + [\mathbf{C}_H])\{\dot{\mathbf{u}}\} + [\mathbf{K}]\{\mathbf{u}\} = \{\mathbf{F}_{ce}\} + \{\mathbf{F}_{co}\} + \{\mathbf{F}_r\}, \tag{7}$$

where $\{\ddot{\mathbf{u}}\}$, $\{\dot{\mathbf{u}}\}$, and $\{\mathbf{u}\}$ are the nodal acceleration, velocity, and displacement vectors, respectively. The structural mass, damping, and stiffness matrices are $[\mathbf{M}] = \int \rho_s[\mathbf{N}]^{\mathrm{T}}[\mathbf{N}]\,dV$, $[\mathbf{C}] = \int c[\mathbf{N}]^{\mathrm{T}}[\mathbf{N}]\,dV$, and $[\mathbf{K}] = \int[\mathbf{B}]^{\mathrm{T}}[\mathbf{D}][\mathbf{B}]\,dV$, respectively. The hydrodynamic added mass and hydrodynamic damping matrices are $[\mathbf{M}_H] = \rho\int[\mathbf{N}]^{\mathrm{T}}[\mathbf{H}][\mathbf{T}]\,dS$ and $[\mathbf{C}_H] = \rho\int[\mathbf{N}]^{\mathrm{T}}[\mathbf{V}_{\mathrm{in}}\cdot\nabla\mathbf{H}][\mathbf{T}]\,dS$, respectively. The nodal force vectors on the right-hand side of Eq. (7) are, respectively, the centrifugal force ($\{\mathbf{F}_{ce}\} = \int \rho_s[\mathbf{N}]^{\mathrm{T}}\{-\boldsymbol{\Omega}\times(\boldsymbol{\Omega}\times(\mathbf{x}+\mathbf{u}))\}\,dV$), Coriolis force ($\{\mathbf{F}_{co}\} = \int \rho_s[\mathbf{N}]^{\mathrm{T}}\{-2\boldsymbol{\Omega}\times\dot{\mathbf{u}}\}\,dV$), and the hydrodynamic force due to rigid blades rotating in asymmetric wake ($\{\mathbf{F}_r\} = \int[\mathbf{N}]^{\mathrm{T}}\{\mathbf{P_r}\}\,dS$). In the current formulation, the influence of fluid–structure interaction has been accommodated by superimposing the hydrodynamic added mass $[\mathbf{M}_H]$ and the hydrodynamic damping $[\mathbf{C}_H]$ matrices, respectively, on to the structural mass $[\mathbf{M}]$ and structural damping $[\mathbf{C}]$ matrices, and by iterating between the fluid and structure solvers to account for nonlinear blade deformation effects.

In these vector and matrix representations, ρ, ρ_s, and c are the fluid density, the solid density, and the solid damping, respectively; $[\mathbf{N}]$, $[\mathbf{B}] = \partial[\mathbf{N}]$, $[\mathbf{D}]$, and $[\mathbf{H}]$ are the displacement interpolation matrix, strain–displacement matrix, material constitutive matrix, and combined influence coefficient matrix from the boundary element method (BEM) calculations, respectively; $[\mathbf{V}_{\mathrm{in}}]$ and $\boldsymbol{\Omega} = [-\omega, 0, 0]^{\mathrm{T}}$ are the effective inflow velocity vector in the rotating blade-fixed coordinates and rotational velocity vector, respectively. The rigid blade hydrodynamic pressure, $P_r = \rho[0.5|\mathbf{V}_{\mathrm{in}}|^2 - \partial\phi/\partial t - 0.5|\mathbf{V}_{\mathrm{in}} + \nabla\phi|^2]$, is defined in terms of the perturbation velocity potential due to the rigid blade rotation (ϕ). The boundary value problem (BVP) for the velocity potential ϕ is solved using a low-order potential-based BEM (Young, 2007, 2008).

The solution procedure involves first computing the hydrodynamic pressure $\mathbf{P_r}$ due to rigid blades rotating in a non-uniform wake, and the hydrodynamic added mass $[\mathbf{M}_H]$ and hydrodynamic damping $[\mathbf{C}_H]$ matrices using the BEM solver. The commercial finite element method, ABAQUS/implicit (ABAQUS, 2005) is used to compute the transient structural response with user-defined functions to incorporate $\mathbf{P_r}$, $[\mathbf{M}_H]$, and $[\mathbf{C}_H]$ (Young, 2007, 2008). Note that the centrifugal $\{\mathbf{F}_{ce}\}$ and Coriolis $\{\mathbf{F}_{co}\}$ body forces are applied as element-based loads in ABAQUS. The deformed blade geometry is fed directly into the BEM solver to obtain the modified geometric influence coefficient matrices and to update the hydrodynamic pressure distribution. Iterations are carried out between the BEM and FEM solvers to account for nonlinear blade deformation effects. For spatially varying inflow, the direct cyclic algorithm in ABAQUS is applied to calculate the transient blade response.

4. Design examples

To examine the feasibility of performance enhancement, and to demonstrate the effectiveness of the proposed design strategy, sample designs are shown in this section. Material and geometry designs are carried out for a specific propeller prototype. Steady and unsteady evaluations are then performed using the designed self-twisting propeller. Satisfaction of design criteria are checked. Insights from the design process are identified.

4.1. Material and geometry designs

Following the design strategy proposed in Section 2, material and geometry designs are carried out for a realistic self-twisting composite propeller. The material design problem has been formulated in Section 2.3.1 as given in Eq. (2). In the current work, an enhanced genetic algorithm (Plucinski et al., 2007) is employed to solve the constrained optimization problem. For simplicity, only the ply orientations and stacking sequence are considered as design variables; all laminae are assumed to have equal thickness and made of the same material with the following properties: $E_L = 139$, $E_T = 8.06$, $G_{LT} = 4.88\,\mathrm{GPa}$, $\nu_{LT} = 0.265$, and $\rho_s = 1750\,\mathrm{kg/m^3}$. The parameter values in Eq. (2) for the optimization problem are taken to be: $\xi = 0.5$, $m_{\max} = 2$, $\lambda_1 = 4$, and $\lambda_2 = 0.5$. The number of layers is taken to be 10 with symmetric configuration for simplicity. Hence, the parametric space has five variables θ_i, $i = 1, \ldots, 5$.

The discrete domain of θ_i is defined to be $\{-15^\circ, 0^\circ, 15^\circ, 30^\circ, 45^\circ, 60^\circ, 75^\circ, 90^\circ\}$, which is chosen to represent the practical range of ply orientation angles, and to reduce the material design to a discrete, binary optimization problem.

Two function evaluators are tested and compared in the optimization simulations with the objective to search for an efficient auxiliary function evaluator for the preliminary design. One of the function evaluators is the simplified plate model presented in Section 3.1 and the other one is the fully integrated BEM–FEM numerical solver presented in Section 3.2. The simplified plate model is applied first, based on the fact that there exists a strong correlation between the twisting rate calculated from the simplified cantilevered plate model, and the change in pitch angles calculated from the realistic propeller blade (Liu and Young, 2007). This plate-GA simulation allows for fine-tuning of controlling parameters for the genetic algorithm, something that would be too time-consuming to do using the second stage full GA simulation. The second stage full GA simulation utilizes the coupled BEM–FEM propeller fluid–structure interaction analysis solver as the function evaluator. The results from the plate-GA and BEM–FEM-GA are presented below.

In the plate-GA, the plate has a length of $a = 1.0\,\text{m}$, width of $b = 0.1\,\text{m}$, and thickness of $t = 0.05\,\text{m}$. The applied moment is taken to be $M = 10\,\text{kN m}$. It should be mentioned that the specific choice of these geometry and loading parameters only influences the absolute value of the deformations for the plate-GA model. It has no influence on the optimization convergence history and resultant stacking sequence since the objective is to maximize the twisting rate per unit load. Hence, it is not necessary to match the values with those of a realistic propeller. The BEM–FEM-GA is performed on the mean-load geometry G_0, which is based on that of propeller 5474. Propeller 5474 is one of the composite propellers manufactured by AIR Fertigung-Technologie GmbH and designed in cooperation with the Naval Surface Warfare Center, Carderock Division (NSWCCD). The propeller has a diameter of $D = 0.61\,\text{m}$. The design advance coefficient is $J = 0.66$ and the design revolution per minute is $n = 780\,\text{rpm}$. More details of propeller 5474 can be found in Chen et al. (2006). A linear pitch alteration is applied to ensure that G_0 is optimal under the design flow condition. A mathematical expression for this scheme can be written as

$$\phi(r) = \phi_0(r) + \Delta\phi(r - R_0)/(R - R_0), \tag{8}$$

where $\phi_0(r)$ is the original pitch angle at radius r, $\Delta\phi$ is the change in tip pitch angle, and R_0 and R are the hub and propeller radii, respectively. Notice that $\phi(R_0) = \phi_0(R_0)$ and $\phi(R) = \phi_0(R) + \Delta\phi$.

The convergence plot for the plate-GA optimization run is shown on the left of Fig. 5. The GA converges after about 60 generations, and the final optimal fiber orientation angles are $\theta = [15^\circ/15^\circ/0^\circ/0^\circ/90^\circ]_s$. It should be pointed out that the bending constraints significantly limit the maximum achievable twisting rate. The maximum twisting rate with bending constraints is only 40% of that without the bending constraints. However, constraints on the number of consecutive layers are much less influential. The convergence plot for the BEM–FEM-GA optimization is shown on the right of Fig. 5. The GA converges within 20 generations, and the optimal fiber orientation angles are $\theta = [15^\circ/15^\circ/0^\circ/0^\circ/30^\circ]_s$, which is remarkably close to that found in the previous plate-GA simulation. The plate-GA follows a slightly different path than the BEM–FEM-GA, despite the same set of genetic algorithm parameters for both models. The steeper ascending rate and quicker leveling-off are evidence of a smaller pool of feasible configurations (that satisfy the constraints), suggesting that the bending constraints, although the same, are tighter in the case of the realistic propeller due to the geometric nonlinearity introduced by the propeller rake and skew. While the plate-GA optimization run requires only a few seconds, the full BEM–FEM-GA optimization run requires around 100 CPU hours on the same SUN BLADE 2000 workstation. Hence, the simplified plate model developed in the current work can be used as an efficient auxiliary function evaluator for the preliminary design of self-twisting composite propellers.

The first-level material design yields the constrained optimal material configuration. This material configuration is then used as input for the second-level geometry design, which then determines the no-load geometry based on the methodology presented in Section 2.3.2. The resultant geometry design is shown in Fig. 6, where the 'undeformed' geometry refers to no-load geometry G_N and the 'deformed' geometry refers to the mean-load geometry G_0. Details of the no-load and mean-load geometries are shown on the right of Fig. 6. At the design flow condition, the no-load geometry will deform to the mean-load geometry as required by the design criteria.

4.2. Performance evaluations

To assess the outcome of the constrained optimal design, the performance of the designed self-twisting composite propeller is then evaluated using the coupled BEM–FEM numerical tool as presented in Section 3.2 under a range of operation conditions.

For steady flow, the pitch angle profiles of the rigid and the (deformed and undeformed) self-twisting propeller at varying Js are shown in Fig. 7. At the design flow condition ($J = J_0 = 0.66$), the pitch angle profile of the flexible propeller deforms to that of the rigid propeller as required by the design criteria. For over-loaded conditions (e.g., $J = 0.50$), the flexible propeller undergoes higher deformation leading to a pitch angle profile below the rigid case due to

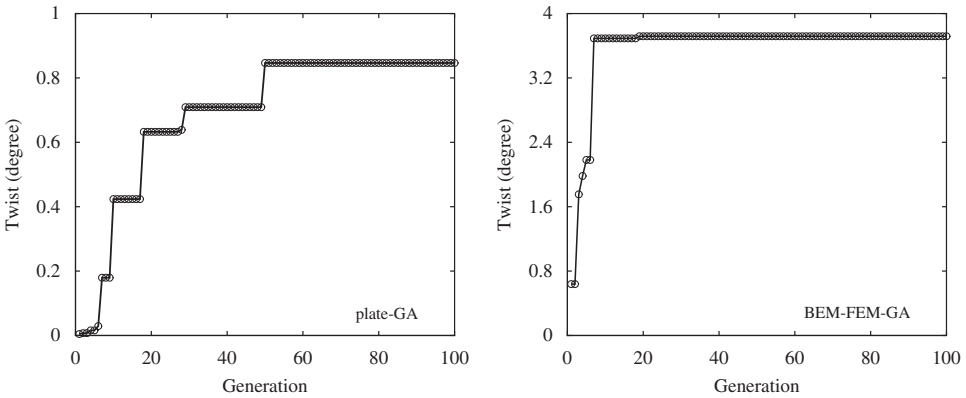

Fig. 5. Comparisons of convergence histories between the plate-GA (left) and BEM–FEM-GA (right) simulations.

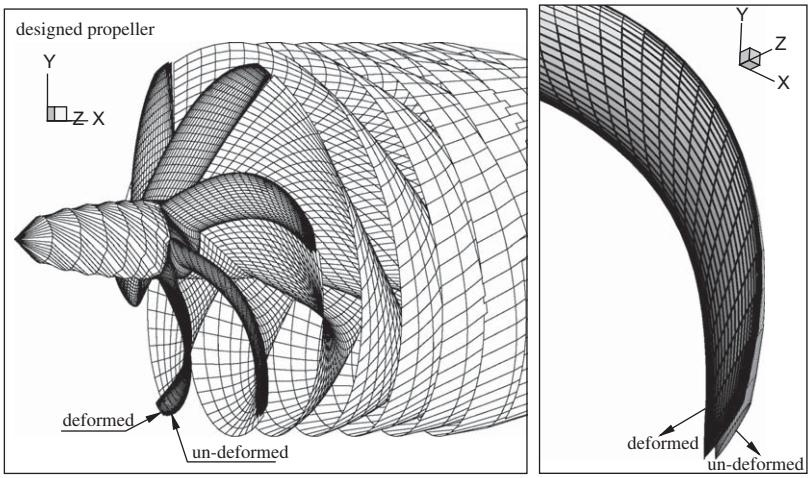

Fig. 6. Undeformed and deformed geometries of the newly designed self-twisting propeller at the design condition ($J = V/nD = 0.66$, $n = 780$ rpm). Left: full propeller structure; right: single blade details.

the higher dimensional hydrodynamic load. For under-loaded conditions (e.g., $J = 0.90$), on the contrary, the flexible propeller undergoes less deformation leading to a higher pitch angle profile due to the lower dimensional hydrodynamic load. On the left side of Fig. 8, the pitch adaptation diagram across a range of J is shown for steady (spatially uniform), open flow condition. The tip pitch angle has been chosen to represent the pitch angle profile for clarity. It can be seen that the deformed pitch angle for the optimized self-twisting propeller bridge the gap between the rigid propeller and the theoretical optimal values. This pitch adaptation behavior is the source of performance enhancement of flexible composite propellers. The comparison of the efficiency ($\eta = K_T J/2\pi K_Q$, where K_T is the thrust coefficient and K_Q the torque coefficient) between the rigid and flexible composite propellers is shown on the right side of Fig. 8. Also shown is the optimal efficiency curve, which represents the maximum achievable efficiency for each J. It can be seen that, the rigid and flexible propeller efficiencies match at the design flow condition $J = 0.66$, as required by the first design criteria. Moreover, the efficiencies of the flexible propeller are higher than its rigid counterpart in off-design conditions ($J \neq 0.66$), which satisfies the second design criteria. The efficiency improvement over the rigid system increases as the flow condition further deviates from the design condition.

To examine the unsteady performance, both propellers are subject to a four-cycle wake, as shown in Fig. 9, at the design flow condition $J = 0.66$ and $n = 780$ rpm. As shown on the left side of Fig. 10, the hydrodynamic axial force (K_{Fx}) and bending moment (K_{Mz}) coefficients vary with the blade angle due to the spatially varying (non-uniform) wake. Also shown are the force and moment coefficients for the rigid propeller. As can be seen, the average values of the flexible and rigid blade force and moment coefficients are approximately the same at the design flow condition. Though the design criteria are only strictly satisfied for steady operations, the designed flexible propeller yields similar

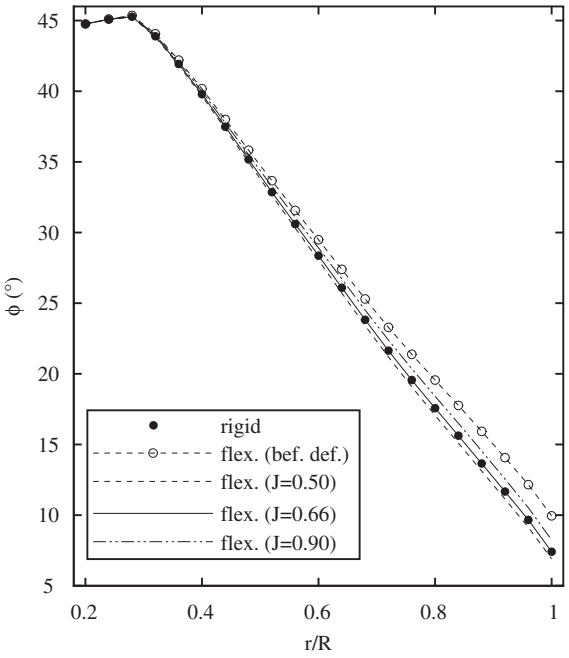

Fig. 7. Pitch angle distribution of the designed self-twisting propeller (steady open water flow, $n = 780$ rpm).

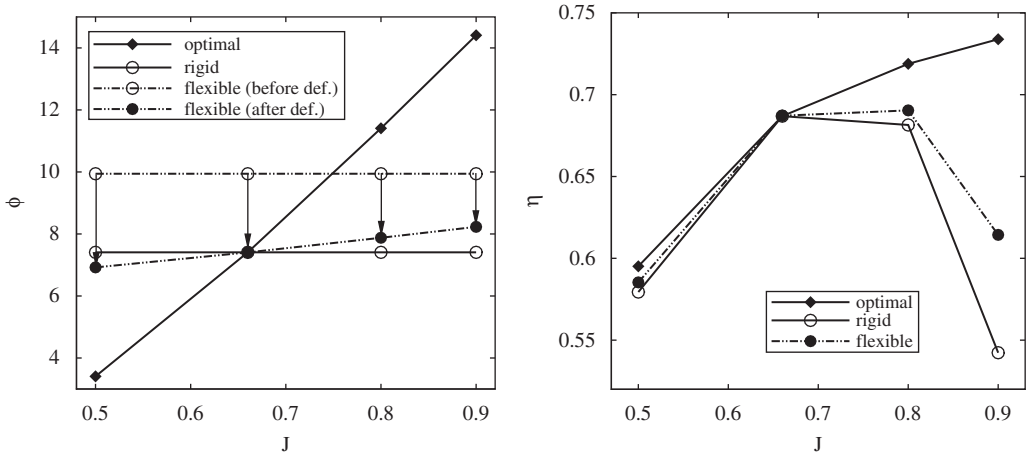

Fig. 8. Left: pitch angle for the new self-twisting propeller design; right: efficiency for the new self-twisting propeller design (steady open water flow, $n = 780$ rpm).

zeroth-order (mean) unsteady behavior as the rigid propeller at the design flow condition. Due to periodic load variations, the deformation and stress levels for the flexible propeller vary correspondingly with the blade angle as shown on the right of Fig. 10. Comparisons of the predicted key (reference) blade and shaft harmonics for the rigid and the flexible propellers at $J = 0.66$ and $n = 780$ rpm are shown on the left and right sides of Fig. 11, respectively. Similar to the open water performance, the zeroth harmonics (mean) of the flexible propeller approximately match those of the rigid propeller under design conditions, though there exist higher-order discrepancies due to flow-induced bending and twisting fluctuations of the flexible propeller.

To demonstrate load-dependent deformation coupling behavior, the normalized axial inflow velocity, change in tip pitch angle ($\Delta\phi$), change in tip skew angle (Δ_{skew}), maximum stresses and deformations, as well as force and moment

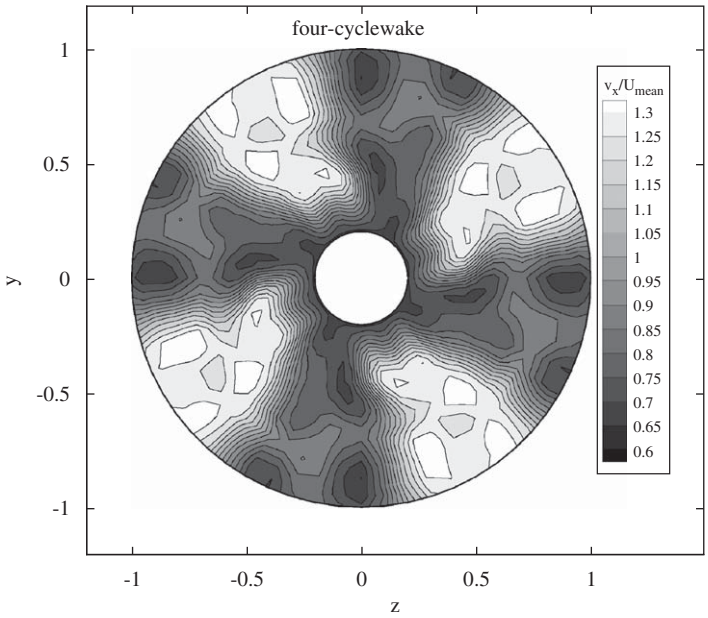

Fig. 9. Axial velocity distribution of the four-cycle wake.

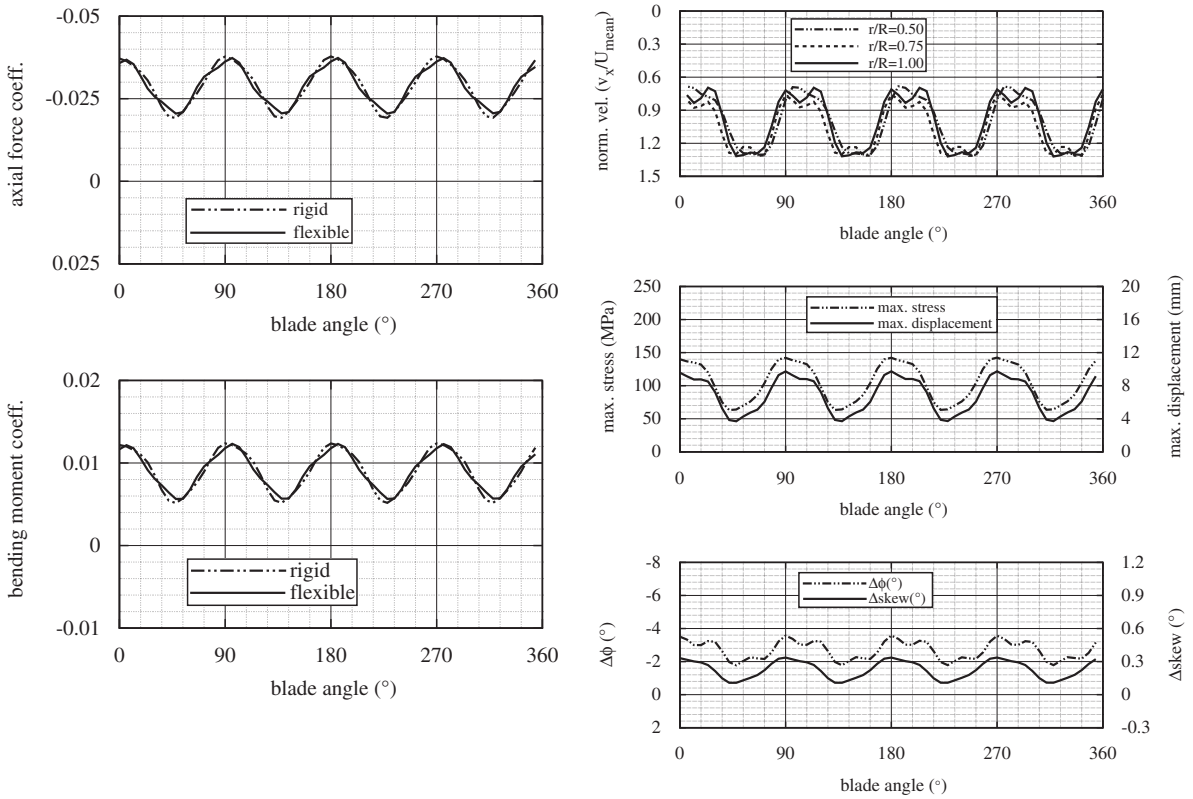

Fig. 10. Left: variation of axial force and bending moment coefficients with blade angles; right: variation of the normalized axial inflow velocities, maximum von Mises stresses and displacement amplitudes, and maximum change in pitch and skew angle at the blade tip ($J = 0.66$, $n = 780$ rpm).

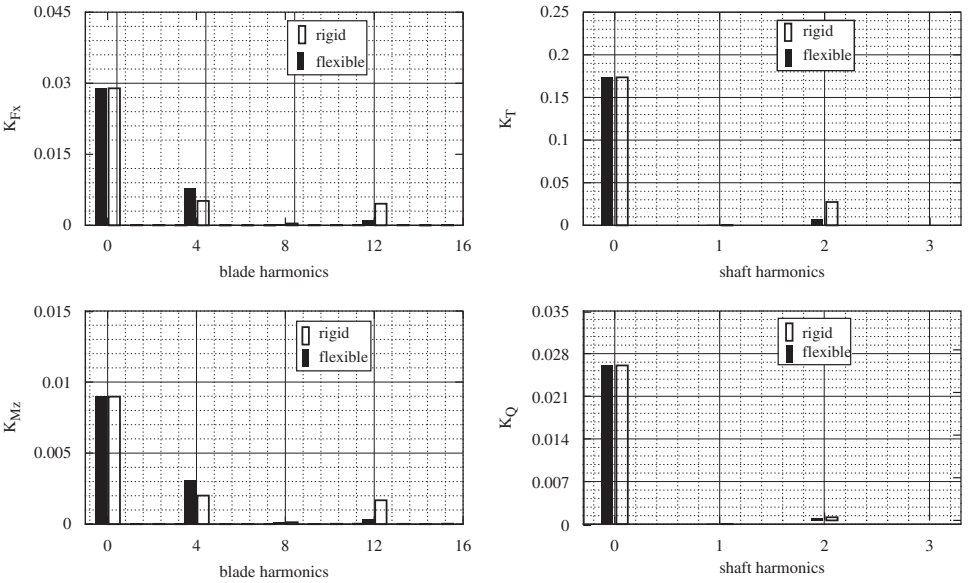

Fig. 11. Left: comparison of the predicted key blade harmonics between the rigid and flexible propellers; right: comparison of the predicted shaft harmonics between the rigid and flexible propellers ($J = 0.66$, $n = 780$ rpm).

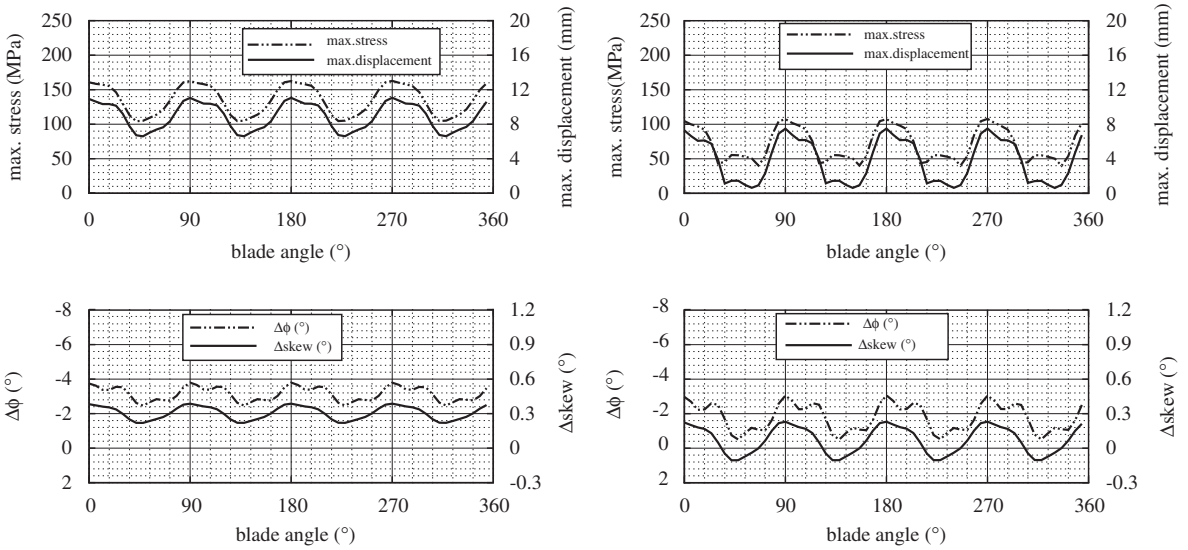

Fig. 12. Variation of deformation and stress variables with blade angles for the flexible propeller (left: $J = 0.50$; right: $J = 0.90$).

coefficients are shown from Figs. 12–14. For comparison purposes, the over-loaded ($J = 0.50$) and under-loaded ($J = 0.90$) cases are shown in parallel. It can be seen from Fig. 12 that the over-loaded propeller has much higher stress level and deformation than the under-loaded case. This is mainly due to higher hydrodynamic loads on the over-loaded propeller blade as can be seen from Figs. 13 and 14. Also shown in Figs. 13 and 14 are the force components compared to the rigid propeller. It is important to note that for over-loaded conditions (e.g., $J = 0.50$), the hydrodynamic loading on the flexible propeller is lower than on the rigid propeller; on the contrary, for under-loaded conditions (e.g., $J = 0.90$), the hydrodynamic loading on the flexible propeller is higher. This can be explained by the pitch adaptation diagram as previously shown on the left of Fig. 8. This load-dependent deformation coupling behavior is the source of

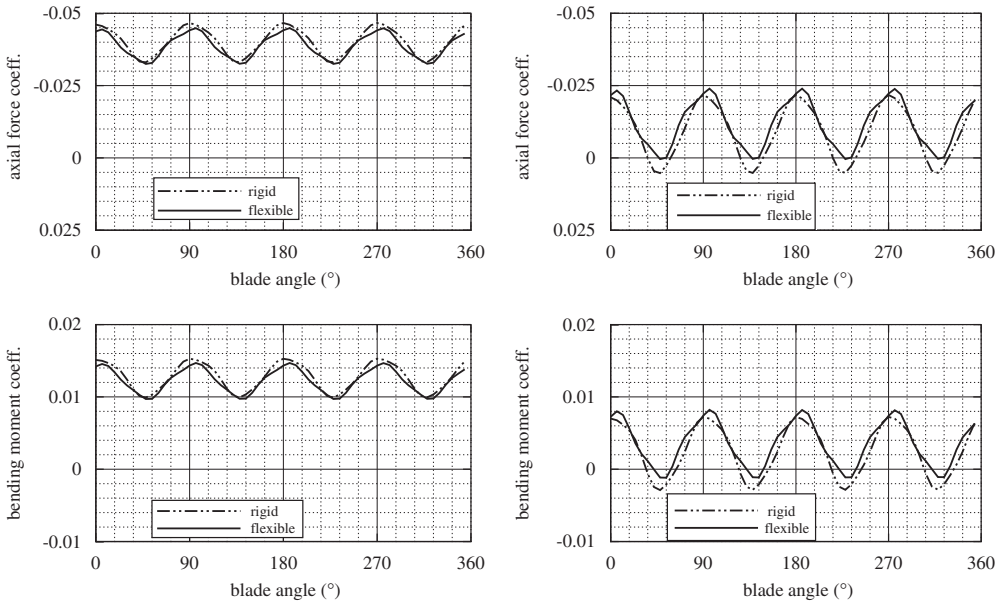

Fig. 13. Variation of axial force and bending moment coefficients with blade angles for the flexible propeller (left: $J = 0.50$; right: $J = 0.90$).

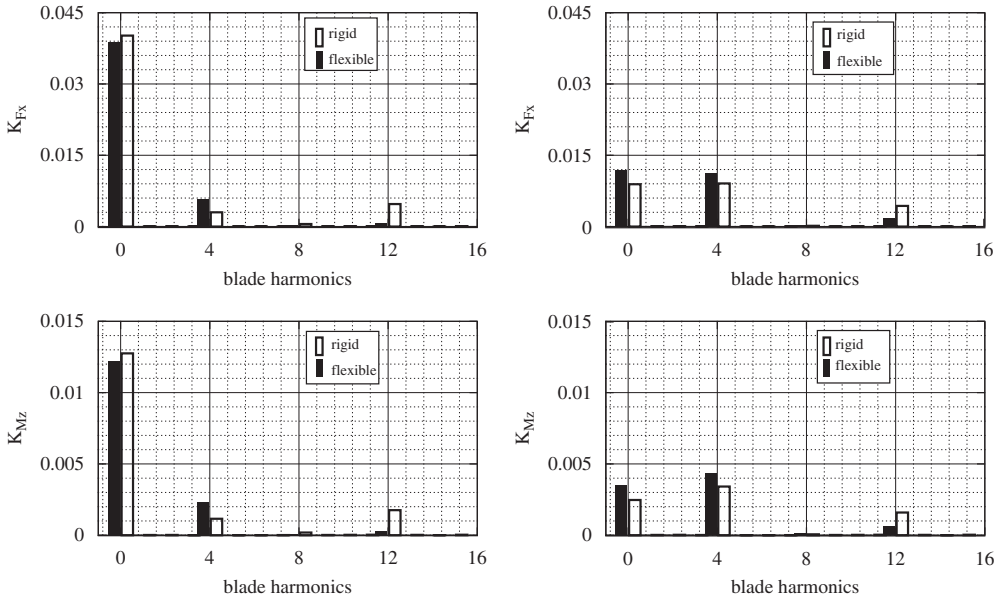

Fig. 14. Comparison of the predicted shaft harmonics between the rigid and flexible propellers (left: $J = 0.50$; right: $J = 0.90$).

performance enhancement of self-twisting composite propellers. The resultant steady and unsteady efficiency improvement (difference in efficiency between the flexible and rigid propellers) is shown in Fig. 15. Slight efficiency improvement behind the spatially varying wake (as shown in Fig. 9) can be discerned from Fig. 15 at the design flow condition ($J = 0.66$). This is true since the effective angle of attack, or instantaneous J for unsteady flow, varies with blade angle for the self-twisting composite propeller, and any deviation from the design J leads to an increase in efficiency, as evidenced in the steady simulation. Under off-design conditions, the flexible self-twisting composite propeller experiences efficiency improvement for both steady and unsteady flows. Moreover, the efficiency improvement

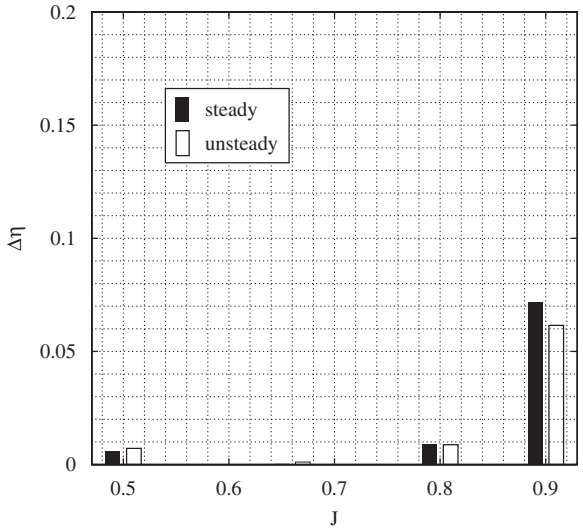

Fig. 15. Efficiency improvement for the newly designed self-twisting propeller ($n = 780$ rpm).

increases as the flow condition further deviates from the design flow condition. This is mainly due to the load-dependent pitch adaptation behavior as explained above.

5. Conclusions

The current work proposed, formulated, and implemented a systematic design methodology to utilize bend–twist coupling effects for performance enhancement of self-twisting composite marine propellers. The design criteria have two aspects: (i) the self-twisting propeller should perform the same as the equivalent rigid propeller at the design flow condition and (ii) the self-twisting propeller should outperform its rigid counterpart under off-design flow conditions, namely, higher efficiency for the self-twisting propeller. To satisfy the design criteria, the proposed design strategies feature a two-level design. The first level is the material design, which is formulated as a constrained optimization problem. The optimization problem is implemented using an enhanced genetic algorithm with binary tree memory and local improvement. Two function evaluators, one of which is a simplified plate model developed in the current work and the other is a BEM–FEM numerical fluid–structure interaction solver validated in previous work (Young, 2007, 2008), are employed and compared. Similar optimal material configurations are obtained from both function evaluators. The simplified plate model significantly speeds up the optimization process and hence can be used as an efficient auxiliary function evaluator for the preliminary design of self-twisting composite propellers. The second level is the geometry design, which is formulated as an inverse problem where the deformed geometry is known but the undeformed geometry is to be determined. An over-relaxed nonlinear iteration procedure is proposed to solve the inverse problem and obtain the no-load geometry. An initial guess for the no-load geometry is taken to be the mean-load geometry. The intermediate deformed geometry due to fluid–structure interactions is then calculated using a coupled BEM–FEM numerical solver (Young, 2007, 2008). The iteration is repeated until the deformed geometry matches the mean-load geometry at the design flow condition. To speed up the convergence, an over-relaxation factor is adopted.

A sample design is provided to illuminate the design strategies and to demonstrate the feasibility of performance enhancement. Steady and unsteady performance evaluations are carried out for the designed self-twisting composite propeller. Results show that a properly designed self-twisting composite propeller can yield higher efficiency than its rigid counterpart at off-design conditions, including behind a spatially varying wake.

Acknowledgments

The authors are grateful to the Office of Naval Research (ONR) and Dr Ki-Han Kim (program manager) for their financial support through Grant nos. N00014-05-1-0694 and N00014-07-1-0491.

References

ABAQUS, 2005. ABAQUS Version 6.5 Documentation. ABAQUS, Inc., Pawtucket, RI 02860, USA.

Chen, B., Neely, S., Michael, T., Gowing, S., Szwerc, R., Buchler, D., Schult, R., 2006. Design, fabrication and testing of pitch-adapting (flexible) composite propellers. In: The SNAME Propeller/Shafting Symposium, VA, September.

Cho, J., Lee, S.C., 1998. Propeller blade shape optimization for efficiency improvement. Computers and Fluids 27, 407–419.

Fukunaga, H., Sekine, H., 1994. A laminate design for elastic properties of symmetric laminates with extension–shear or bending–twisting coupling. Journal of Composite Materials 28 (8), 708–731.

Gowing, S., Coffin, P., Dai, C., 1998. Hydrofoil cavitation improvements with elastically coupled composite materials. In: Proceedings of 25th American Towing Tank Conference, Iowa city, IA, USA.

Green, J., 1987. Aeroelastic tailoring of aft-swept high-aspect-ratio composite wings. Journal of Aircraft 24 (11), 812–819.

Howe, M.S., 2007. The genetically optimized tunnel-entrance hood. Journal of Fluids and Structures 23, 1231–1250.

Hwang, S., Gibson, R., 1993. Influence of bending–twisting and extension–bending coupling on damping of laminated composites. Journal of Materials Science 28, 1–8.

ITTC, 2005. Final report and recommendations to the 24th ITTC by the Propulsion Committee. In: Proceedings of the 24th ITTC, vol. I. Edinburgh, United Kingdom, pp. 73–136.

Kane, C., Smith, J., 2003. Composite blades in marine propulsors. In: Proceedings of International Conference on Advanced Marine Materials: Technologies and Applications, RINA, London, UK.

Khan, A., Adams, D., Dayal, V., Vogel, J., 2000. Effects of bend–twist coupling on composite propeller performance. Mechanics of Composite Materials and Structures 7, 383–401.

Khot, N.S., Zweber, J.V., 2003. Design of flutter characteristics of composite wings using frequency constraint optimization. Journal of Aerospace Engineering 16, 19–30.

Kogiso, N., Watson, L., Gurdal, Z., Haftka, R., 1993. Genetic algorithms with local improvement for composite laminate design. Technical Report, Department of Computer Science, Virginia Polytechnic Institute and State University, Blacksburg, VA, USA.

Kogiso, N., Watson, L., Gurdal, Z., Haftka, R., Nagendra, S., 1994. Design of composite laminates by a genetic algorithm with memory. Technical Report, Department of Computer Science, Virginia Polytechnic Institute and State University, Blacksburg, VA, USA.

Lee, Y., Lin, C., 2004. Optimized design of composite propeller. Mechanics of Advanced Materials and Structures 11, 17–30.

Lin, C., Lee, Y., 2004. Stacking sequence optimization of laminated composite structures using genetic algorithm with local improvement. Composite Structures 63, 339–345.

Lin, G., 1991. Three dimensional stress analyses of a fiber-reinforced composite thruster blade. In: The SNAME Propeller/Shafting Symposium, Virginia Beach, VA, USA.

Lin, H., Lin, J., 1997. Effect of stacking sequence on the hydroelastic behavior of composite propeller blades. In: 11th International Conference on Composite Materials. Australian Composite Structures Society, Gold Coast, Australia, July 14–18.

Liu, Z., Young, Y.L., 2007. Utilization of deformation coupling in self-twisting composite propellers. In: Proceedings of 16th International Conference on Composite Materials, Kyoto, Japan.

Marques, F.D., Anderson, J., 2001. Identification and prediction of unsteady transonic aerodynamic loads by multi-layer functionals. Journal of Fluids and Structures 15, 83–106.

Plucinski, M.M., Young, Y.L., Liu, Z., 2007. Optimization of a self-twisting composite marine propeller using a genetic algorithms. In: Proceedings of 16th International Conference on Composite Materials, Kyoto, Japan.

Soykasap, O., Hodges, D., 2000. Performance enhancement of a composite tilt-rotor using aeroelastic tailoring. Journal of Aircraft 37 (5), 850–858.

VanGoethem, D., Radford, D., 2004. Design of structurally coupled composite beams under combined bending and tension loading. In: 36th International SAMPLE Technical Conference—Materials and Processing: Sailing into the Future, San Diego, CA, USA, November 15–18.

Yamane, T., 1992. Aeroelastic tailoring analysis for advanced turbo propellers with composite blades. Computers and Fluids 21 (2), 235–245.

Yamane, T., Peretz, F., 1993. Aeroelastic tailoring analysis for preliminary design of advanced propellers with composite blades. Journal of Aircraft 30 (1), 119–126.

Young, Y.L., 2007. Time-dependent hydroelastic analysis of cavitating propellers. Journal of Fluids and Structures 23, 269–295.

Young, Y.L., 2008. Fluid–structure interaction analysis of flexible composite marine propellers. Journal of Fluids and Structures 24, 799–818.

Young, Y.L., Liu, Z., 2007. Hydroelastic tailoring of composite naval propulsors. In: 26th International Conference on Offshore Mechanics and Arctic Engineering, San Diego, CA, USA.

Ziaei-Rad, S., Ziaei-Rad, M., 2006. Inverse design of supersonic diffuser with flexible walls using a genetic algorithm. Journal of Fluids and Structures 22, 529–540.